J.WINCZEK*, T. SKRZYPCZAK*,#

THERMOMECHANICAL STATES IN ARC WELD SURFACED STEEL ELEMENTS

The paper presents a model of temperature, phase transformation and stresses fields in a steel element during single-pass Gas Metal Arc Weld (GMAW) surfacing.

Kinetics of phase transformations during heating is limited by temperature values at the beginning and at the end of austenitic transformation, while the progress of phase transformations during cooling is determined on the basis of TTT-welding diagram and Johnson-Mehl-Avrami and Kolomogorov law for diffusive transformations and Koistinen-Marburger for martensitic transformation. Stress state of a bar subjected to thermo-mechanical loads is described assuming the plane cross section hypothesis and using integral equations of stress equilibrium of a bar as well as simple Hook's law. Stresses in the elastic-plastic state are determined by iteration using solutions with a variable elastic modulus of elasticity, conditioned by tensile curves. Dependence of stresses on strains is assumed on the basis of tensile curves of particular structures, taking into account the influence of temperature. There were performed calculations of the temperature field, phase transformations, strains and stresses for GMAW surfacing of a cuboid element made of S235 steel. Authors' programs, made in Borland Delphi, were used for calculations.

Keywords: Temperature field, Phase transformation, Gas Metal Arc Weld surfacing

1. Introduction

Plastic strains and residual stresses have essential influence on the characteristics of welded steel product during its exploitation. A quantitative description of the changes in strains and stresses during welding is difficult and needs to take into account the complicated thermal processes and the dependence of thermo-mechanical properties on temperature [1]. The simplified estimation methods of residual stress distribution for the typical welded joint were introduced in [2, 3] among others.

The complete modelling of thermomechanical phenomena occurring during welding should consist of changeable temperature field, phase transformations as well as stress and strain states connected by a constitutive law. Such approach is reflected i.a. in works [4 - 9], where modelling of temperature fields, phase transformations and strain states have been carried out with the use of numerical methods (eg. FEM). Analytical methods are useful in analysis of the formation and development of plastic strain and stress as well as building the simplified schemes of residual stress distributions because they allow to evaluate quickly the stress field and the influence of plasticity zones on the residual stresses.

In the modelling of temperature field of welding processes a single-distribution heat source model, reflecting the direct impact of the electric arc on the surfaced object, is generally assumed. This approach is found in the description of the temperature field during welding processes using analytical and numerical methods [10 -14]. Fusion lines in arc weld surfacing often exhibit shape irregularity that is difficult to

obtain by means of the single-distributed heat source model in the description of the temperature field. Therefore a double distribution model was proposed, finding justification in the process of transferring heat to the surfaced object.

2. The model of temperature field

The model assumes a physically single heat source - the electric arc. Whereas, the heat generated by the electric arc is divided into a part transmitted to the surfaced object by the direct influence of the electric arc, and a part of the heat in the molten material of the electrode, which in the form of drops, under the influence of electromagnetic forces and gravity, is transferred to the resulting weld. This material, after mixing in the weld pool, with the molten material of the surfaced object constitutes the weld overlay. In the description of the temperature field the solution of a basic heat conduction equation was used. On the basis of solutions for the volume sources, the temperature field during welding was determined by summing up the temperature field caused by the action of the applied weld and an electric arc.

The proposed solution for temperature field is summing temperature fields caused by the heat of direct impact of an electric arc and the heat transferred to the surfaced object through the molten electrode material. It was assumed that the volume of the weld reinforcement and the heat accumulated there are approximately equal to the volume of molten electrode wire and the amount of the heat consumed for melting the electrode. This allows for the formulation of the temperature field in the form:

* CZESTOCHOWA UNIVERSITY OF TECHNOLOGY, FACULTY OF MECHANICAL ENGINEERING AND COMPUTER SCIENCE, 42-201 CZESTOCHOWA, 21 ARMII KRAJOWEJ STR., POLAND
# Corresponding author: skrzyp@imipkn.pcz.czest.pl

$$T(x,y,z,t) - T_0 = T_a(x,y,z,t) + T_w(x,y,z,t) \qquad (1)$$

where: $T_a(x,y,z,t)$ – temperature field caused by the heat of the direct impact of an electric arc,

$T_w(x,y,z,t)$ – temperature field caused by the heat of the weld reinforcement (consumed to melt the electrode).

The shape of the weld face is determined mainly by the forces of surface tension. On the basis of experimental research Hrabe and others [15] have proposed a parabolic shape of the face. Lower limit of the imposed metal is defined by the surface shape of surfaced material. In the solution parabolic model was adopted. Then the geometry of the weld is determined (Fig. 1): where: hw is the height of the weld (weld reinforcement – the

part of the weld above the surface of the surfaced material), dp is the depth of material thickness loss (e.g. depth of wear zone), and Δl results from considering the volume of material supplied from the electrode.
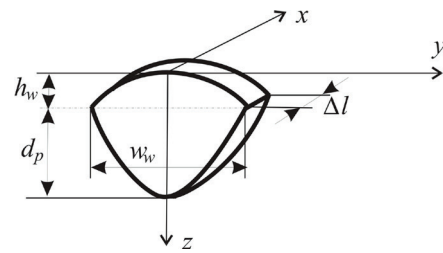

Fig. 1. Geometry of the weld

$$T(x,y,z,z_0,t) - T_0 = A_w \int_0^t \left\{ H_H(t'')\left(F_2(y,z) + F_3(y,z) - F_4(y,z) - F_1(y,z)\right)\right\}dt'' + A_H \int_0^t F_H(t'')dt'' \qquad (2)$$

$$T(x,y,z,z_0,t) - T_0 = A_w \int_0^{t_c} \left\{ H_C(t')\left(G_2(y,z) + G_3(y,z) - G_4(y,z) - G_1(y,z)\right)\right\}dt' + A_C \int_0^{t_c} F_C(t')dt' \qquad (3)$$

$$A_H = \frac{3\dot{q}_2}{16 C_p \rho (\pi a)^{1.5} z_0} \exp\left(-\frac{\xi v}{2a} - \frac{v^2 t_0}{4a}\right) \qquad (4)$$

$$F_H(t'') = \frac{1}{t''+t_0}\exp(-\frac{\xi^2}{4a(t''+t_0)} - \frac{v^2 t''}{4a})$$

$$((1 - \frac{z^2 + 2at''}{z_0^2})(erf(\frac{z+z_0}{2(at'')^{0,5}}) - \Phi(z)erf(\Phi(z)\frac{z-z_0}{2(at'')^{0,5}})) + \qquad (5)$$

$$\frac{4at''}{z_0^2}(\frac{z+z_0}{(4\pi at'')^{0,5}}\exp(-\frac{(z-z_0)^2}{4at''}) - \frac{z-z_0}{(4\pi at'')^{0,5}}\exp(-\frac{(z+z_0)^2}{4at''})))dt''$$

$$A_C = \frac{3}{16}\frac{\dot{q}_2}{C_p \rho \pi a z_0} \qquad (6)$$

$$F_C(t') = \frac{1}{t+t_0-t'}$$

$$\exp(-\frac{(x-vt'-x_0)^2 + (y-y_0)^2}{4a(t+t_0-t')})$$

$$((1 - \frac{z^2 + 2a(t-t')}{z_0^2})(erf(\frac{z+z_0}{2(a(t-t'))^{0,5}}) - \Phi(z)erf(\Phi(z)\frac{z-z_0}{2(a(t-t'))^{0,5}})) + \qquad (7)$$

$$\frac{4a(t-t')}{z_0^2}(\frac{z+z_0}{(4\pi a(t-t'))^{0,5}}\exp(-\frac{(z-z_0)^2}{4a(t-t')}) - \frac{z-z_0}{(4\pi a(t-t'))^{0,5}}\exp(-\frac{(z+z_0)^2}{4a(t-t')})))$$

$$\Phi(z) = \begin{cases} -1 & dla \ z \in <0, z_0> \\ 1 & dla \ z \in (z_0, \infty) \end{cases} \qquad (8)$$

$$A_w = \dot{q}_v / 8C_p \rho \sqrt{\pi a} \tag{9}$$

$$H_H(t'') = \frac{1}{\sqrt{t''}} \left(erf\left(\frac{\Delta l - 2(\xi + vt'')}{4\sqrt{at''}} \right) + erf\left(\frac{\Delta l + 2(\xi + vt'')}{4\sqrt{at''}} \right) \right) \tag{10}$$

$$H_C(t') = \frac{1}{\sqrt{(t-t')}} \left(erf\left(\frac{\Delta l - 2(x - vt' - x_0)}{4\sqrt{a(t-t')}} \right) + erf\left(\frac{\Delta l + 2(x - vt' - x_0)}{4\sqrt{a(t-t')}} \right) \right) \tag{11}$$

$$F_1(y,z) = \frac{w_w}{2} \sum_{i=1}^{n} \left[w_i \exp\left(-\left(\frac{y - \frac{w_w}{2}\upsilon_i}{2\sqrt{at''}} \right)^2 \right) erf\left(\frac{1}{2\sqrt{at''}} \left(z + d_p \upsilon_i^2 - d_p - h_w \right) \right) \right] \tag{12}$$

$$F_2(y,z) = \frac{w_w}{2} \sum_{i=1}^{n} \left[w_i \exp\left(-\left(y - \frac{w_w}{2}\upsilon_i / 2\sqrt{at''} \right)^2 \right) erf\left(\frac{1}{2\sqrt{at''}} \left(z - h_w \upsilon_i^2 \right) \right) \right] \tag{13}$$

$$F_3(y,z) = \frac{w_w}{2} \sum_{i=1}^{n} \left[w_i \exp\left(-\left(\frac{y - \frac{w_w}{2}\upsilon_i}{2\sqrt{at''}} \right)^2 \right) erf\left(\frac{1}{2\sqrt{at''}} \left(z - d_p \upsilon_i^2 + d_p + h_w \right) \right) \right] \tag{14}$$

$$F_4(y,z) = \frac{w_w}{2} \sum_{i=1}^{n} \left[w_i \exp\left(-\left(\frac{y - \frac{w_w}{2}\upsilon_i}{2\sqrt{at''}} \right)^2 \right) erf\left(\frac{1}{2\sqrt{at''}} \left(z + h_w \upsilon_i^2 \right) \right) \right] \tag{15}$$

$$G_1(y,z) = \frac{w_w}{2} \sum_{i=1}^{n} \left[w_i \exp\left(-\left(\frac{y - \frac{w_w}{2}\upsilon_i}{2\sqrt{a(t-t')}} \right)^2 \right) erf\left(\frac{1}{2\sqrt{a(t-t')}} \left(z + d_p \upsilon_i^2 - d_p - h_w \right) \right) \right] \tag{16}$$

$$G_2(y,z) = \frac{w_w}{2} \sum_{i=1}^{n} \left[w_i \exp\left(-\left(\frac{y - \frac{w_w}{2}\upsilon_i}{2\sqrt{a(t-t')}} \right)^2 \right) erf\left(\frac{1}{2\sqrt{a(t-t')}} \left(z - h_w \upsilon_i^2 \right) \right) \right] \tag{17}$$

$$G_3(y,z) = \frac{w_w}{2} \sum_{i=1}^{n} \left[w_i \exp\left(-\left(\frac{y - \frac{w_w}{2}\upsilon_i}{2\sqrt{a(t-t')}} \right)^2 \right) erf\left(\frac{1}{2\sqrt{a(t-t')}} \left(z - d_p \upsilon_i^2 + d_p + h_w \right) \right) \right] \tag{18}$$

$$G_4(y,z) = \frac{w_w}{2} \sum_{i=1}^{n} \left[w_i \exp\left(-\left(\frac{y - \frac{w_w}{2}\upsilon_i}{2\sqrt{a(t-t')}} \right)^2 \right) erf\left(\frac{1}{2\sqrt{a(t-t')}} \left(z + h_w \upsilon_i^2 \right) \right) \right] \tag{19}$$

Analytical description of the temperature field caused by the direct impact of the electric arc with Gaussian heat distribution (Fig. 2) is shown in [16], whereas considering the heat stored in the liquid metal imposed on the surface is presented in [17]. For accepted scheme of the single-pass surfacing (Fig. 3), the temperature field (1) is defined as follows:

for time $t \leq tc$, where tc is the total time of making of the weld:

$$\xi = x - vt - x_0 \qquad (20)$$

$$t_c = l / v \qquad (21)$$

a - thermal diffusivity [m²/s], C_p - specific heat [J/kg K], ρ - density [kg/m3], x_0 [m] and l [m] are the coordinates of the start and length of the weld respectively. Quantity t_0 [s] characterizes surface heat source distribution, whereas $r_B^2 = 4at_0$ [18] (comp. Fig. 2). Formulas [12-19] are solutions of integrals using Gauss-Legendre quadrature.
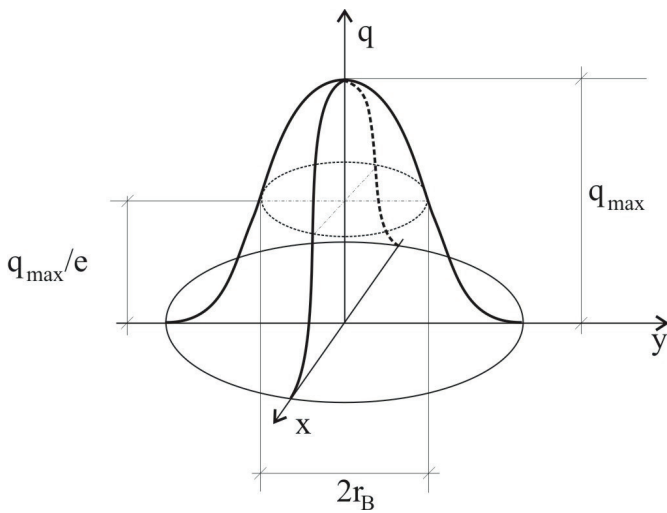

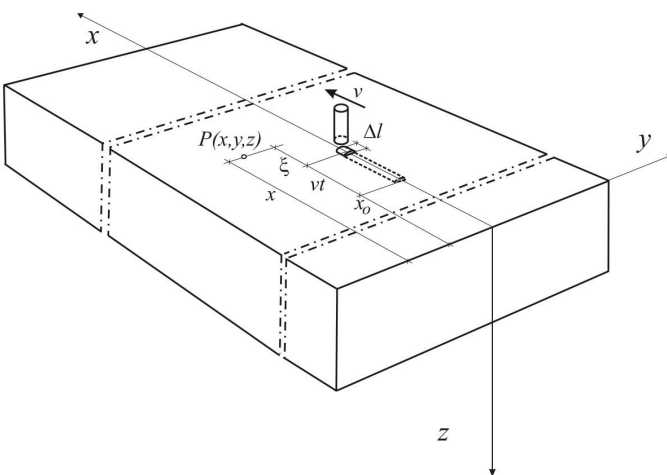Fig. 2. Gaussian distribution of heat source

Fig. 3. Arc weld surfacing scheme

Total amount of heat q_v contained in the material of melted electrode is expressed by the relationship [19]:

$$q_v = \Delta q_{solid} + \Delta q_f + \Delta q_{liqiud} \qquad (22)$$

where:
Δq_{solid} – heat necessary to heat-up the electrode from the initial temperature to the melting temperature, Δq_f – heat used for melting the electrode (heat of fusion), Δq_{liquid} – heat used for heating-up melted material to the temperature, in which the drop of metal falls on the surface of welded material, T_e - the initial temperature of the electrode.

On account of this we get:

$$\dot{q}_v = \dot{m}\left(C_p\left(T_L - T_e\right) + L\right) \qquad (23)$$

where:

$$\dot{m} = \rho_e \frac{\pi d^2}{4} v_e \qquad (24)$$

v_e [m/s] – velocity of passing electrode wire with diameter d [m] and density ρ_e [kg/m³].

3. Kinetcs of phase transforamations in solid state

The type of newly created phase depends heavily on kinetics of heating and cooling processes. Kinetics of those processes are described by Johnson-Mehl-Avrami's and Kolomogorov's (JMAK) rules [20]. The amount of austenite φ_A created during heating the ferrite-pearlitic steel is therefore defined according t

$$\varphi_A(T) = \sum_j \varphi_j^0 \left(1 - \exp\left(-b_j(T)t^{n_j(T)}\right)\right) \qquad (25)$$

where ϕ_j^0 constitutes initial share of ferrite ($j\equiv F$), pearlite ($j\equiv P$) and bainite ($j\equiv B$), while constants b_j and n_j are determined using conditions of the beginning and the end of transformation:

$$n_j = \frac{\ln(\ln(0.99))}{\ln(A_1 / A_3)} \ , \ b_j = \frac{0.01n_i}{A_1} \qquad (26)$$

In welding processes the volume fractions of particular phases during cooling depend on the temperature, cooling rate, and the share of austenite (in the zone of incomplete conversion $0\leq\phi_A\leq1$). In quantitative perspective the progress of phase transformation during cooling is estimated using additivity rule by voluminal fraction ϕ_j of created phase what can be expressed analogically to Avrami's formula [21] by equation:

$$\varphi_j(T,t) = \varphi_A \varphi_j^{max} \left\{1 - \exp\left[b_j\left(T(v_{8/5})\right)t(T)^{n(T(v_{8/5}))}\right]\right\} \qquad (27)$$

where φ_j^{max} is the maximum volumetric fraction of phase j for the determined cooling rate estimated on the basis of the continuous cooling diagram (Fig. 4) while the integral volumetric fraction equals to:

$$\sum_{j=1}^{k} \varphi_j = 1 \qquad (28)$$

and k denotes the number of structural participations.

The quantitative description of dependence of material's structure and quality on temperature and transformation time of over-cooled austenite during surfacing is made using the time-temperature-transformation diagram during continuous

cooling, which binds the time of cooling $t_{8/5}$ (time when material stays within the range of temperature between 500 [°C] and 800 [°C], or the velocity of cooling ($v_{8/5} = (800\text{-}500)/t_{8/5}$) and the temperature with the progress of phase transformation (Fig. 4). Those diagrams are called TTT–welding diagrams.
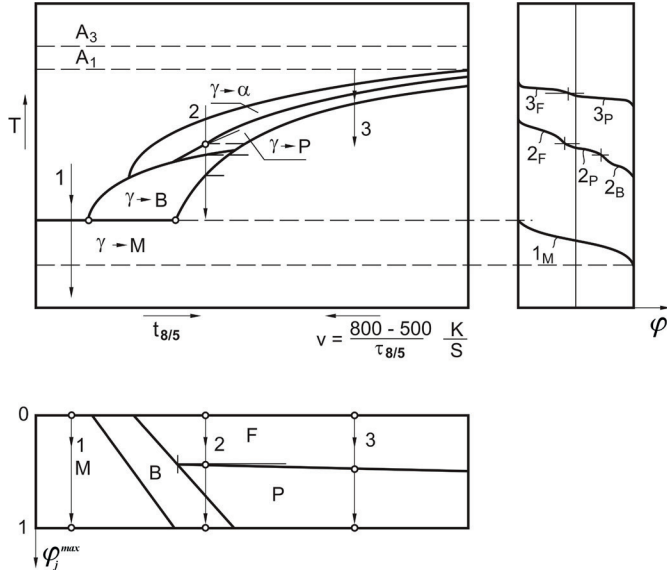

Fig. 4. Scheme of phase changes of overcooled austenite depending on cooling velocity within temperature range 800-500 °C

In quantitative perspective the progress of phase transformation is estimated by volumetric fraction φj of created phase, where i can denote ferrite (jF), pearlite (jP), bainite (jB) or martensite (jM). Volumetric fraction φj of created phase can be expressed using formula (27), in which time t is replaced with new independent variable – temperature T [22]:

$$\varphi_j = \varphi_A \varphi_j^{\max} \left(1 - \exp\left(-b_j T^{n_j}\right)\right) + \varphi_j^0 \qquad (29)$$

where:

$$n_j = \frac{\ln\left(\ln\left(1 - \varphi_j^s\right)/\ln\left(1 - \varphi_j^f\right)\right)}{\ln\left(T_j^s / T_j^f\right)} \quad , \quad b_j = \frac{n_j\left(1 - \varphi_j^f\right)}{T_j^s} \qquad (30)$$

$$\frac{\varphi_j^s}{\varphi_j^{\max}} = 0.01 \qquad \frac{\varphi_j^f}{\varphi_j^{\max}} = 0.99 \qquad (31)$$

φj^0 is volumetric participation of j-th structural component, which has not been converted during the austenitization, $T_j^s = T_j^s(v_{8/5})$ and $T_f = T_f(v_{8/5})$ are respectively initial and final temperature of phase transformation of this component.

The fraction of martensite formed below the temperature M_s is calculated using the Koistinen-Marburger formula [23 - 25]:

$$\varphi_M(T) = \varphi_A / \varphi_M^{\max} \left\{1 - \exp\left[-\mu\left(M_s - T\right)\right]\right\} \; ,$$
$$\mu = -\frac{\ln\left(\varphi_M^{\min} = 0.1\right)}{M_s - M_f} \qquad (32)$$

where ϕ_m denotes volumetric fraction of martensite, M_s and M_f denote initial and final temperature of martensite transformation respectively, T the current temperature of process.

4. Thermal and phase transformation strains

Total strain during single-pass surfacing represents the sum of thermal strains caused by phase transformation during heating and cooling:

$$\varepsilon(x, y, z, t) = \varepsilon^H + \varepsilon^C \qquad (33)$$

where ε^H and ε^C - denote thermal and phase transformation strains during heating and cooling respectively.

Heating leads to the increase in material's volume, while transformation of the initial structure (ferritic, pearlitic or bainitic) in austenite causes shrinkage connected with different density of given structures. Then strains during heating is equal to:

$$\varepsilon^H = \varepsilon^{Th} - \varepsilon^{Trh} \qquad (34)$$

where ε^{Th} is a strain caused by thermal expansion of the material:

$$\varepsilon^{Th} = \sum_{i=A,P,F,B,M} (\alpha_i \varphi_{i0}(T - T_0)H(T_{A_1} - T) + \\ + \alpha_i \varphi_i(T - T_{A_1})H(T_{A_3} - T)H(T - T_{A_1}) + \\ + \alpha_A(T - T_{A_3})H(T - T_{A_3})) \qquad (35)$$

while ε^{Trh} is a phase transformation strain during heating:

$$\varepsilon^{Trh} = \sum_{i=P,F,B,M} \varphi_i \gamma_{iA} \qquad (36)$$

where: γ_{iA} – structural strain of i-th structure in austenite, T_0 – initial temperature, α_i - linear thermal expansion coefficient of i-th structure, and $H(x)$ is the function defined as follows:

$$H(x) = \begin{cases} 1 & for\ x > 0 \\ 0{,}5 & for\ x = 0 \\ 0 & for\ x < 0 \end{cases} \qquad (37)$$

Cooling of material causes its shrinkage, while transformation of austenite in cooling structures causes in turn the increase of its volume. It leads to complicated changes of strains dependent not only on the current temperature of material during cooling but also on the initial and final temperature of transformation of austenite into ferrite, pearlite, bainite or martensite as well as on voluminal shares of given structural constituents (including austenite). The strain during cooling can be described by the relation:

$$\varepsilon^C = \varepsilon^{Tc} + \varepsilon^{Trc} \qquad (38)$$

where ε^{Tc} is the strain caused by thermal shrinkage of material:

$$\varepsilon^{Tc} = \alpha_A(T - T_{SOL})H(T - T_s) + \alpha_A(T_s - T_{SOL})H(T_s - T) + \\ + \sum_{i=A,P,F,B,M} \alpha_i \varphi_i(T - T_{si})H(T_{si} - T) \qquad (39)$$

while ε^{Trc} is the strain caused by phase transformation during cooling,

$$\varepsilon^{Trc} = \sum_{i=P,F,B,M} \varphi_i \gamma_{Ai} \tag{40}$$

where T_{SOL} denotes solidus temperature, T_s – initial temperature of phase transformation, T_{si} - initial temperature of austenite transformation in i-th structure, γ_{Ai} – structural strain of austenite in *i*-th structure. In addition, due to the limit on solid state of material:

$$\varepsilon(x,y,z,t) = 0 \quad for \quad T > T_{SOL} \tag{41}$$

5. Stress states

5.1. Stress states of surfacing with dominant axial stresses

Longitudinally surfaced element whose length is much bigger than its crosswise size is taken into consideration. A prismatic rod subjected to mechanical strains has been used to describe stress state. Separate cross sections x are characterised by internal forces $N = N(x)$ and $M_y = M_y(x)$. Remaining forces are assumed to be negligible (transverse forces: $T_y = T_y(x)$, $T_z = T_z(x)$) or absent ($M_x = M_x(x)$). The rod is also subjected to symmetric action in relation to z axis in slowly changing temperature field $T = T(x,y,z) = T(x,-y,z)$. This field is characterised by low temperature gradient in relation to the variable x. The stress state of the rod is characterised by single dimensional stress state $\sigma x = \sigma x(x,z,t) = \sigma x(x,-y,z,t)$ (Fig. 5). For modulus of longitudinal elasticity changeable towards coordinates (heterogeneous material of surfaced sample) and Young`s modulus $E = E(T)$ dependent on temperature, the stress can be described by [26]:

$$\sigma = \frac{E}{A^E J_y^E - (S_y^E)^2} (J_y^E(N(x)+N^T) + S_y^E(M(x)-M_y^T) + \\ -(A^E(M(x)-M_y^T)+S_y^E(N(x)+N^T))z) - E\varepsilon_0 - \alpha ET \tag{42}$$

where:
$$A^E = \int_{(A)} EdA, \qquad S_y^E = \int_{(A)} EzdA,$$
$$J_y^E = \int_{(A)} Ez^2dA, \quad N^T = \int_{(A)} \alpha ETdA, \qquad M_y^T = \int_{(A)} \alpha ETzdA.$$
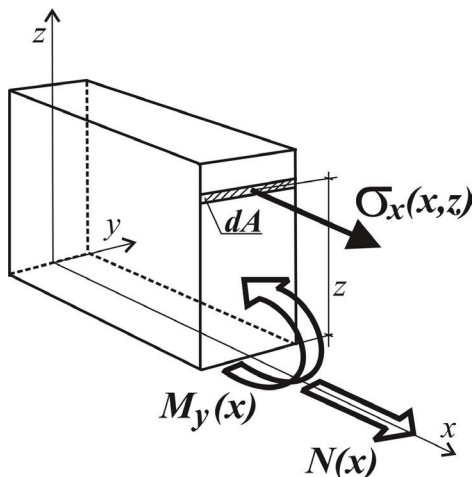
Fig. 5. Scheme of the rod subjected to loads

5.2. The analysis of physical nonlinearity of material

The stresses in elasto-plastic state are determined by iteration using the method of elastic solutions at the variable modulus of longitudinal elasticity conditioned by the stress-strain curve [27]. Applied in the iteration function, $\sigma = f(\varepsilon)$ is obtained by reproduction of the tension and compression curves. Let us denote by σs the border below which unloading does not leave permanent strains. The first solution, which is the beginning of iteration for the determined external load and given permanent strain is obtained on the basis of (43). If the obtained stress for the Young's modulus is in the plastic range ($\left|\sigma_{(1)}\right| > \sigma_S$), then the change in modulus E must be done.

The stress $\sigma_{(1)}$ corresponds to strain:

$$\varepsilon_{(1)} = \sigma_{(1)} / E_{(1)} \tag{43}$$

Stresses $\sigma(1)$ are determined from the stress-strain curve for strain $\varepsilon_{(1)}$, on the basis of which Young's modulus (Fig. 6) is defined:

$$E_{(2)} = \sigma(1) / \varepsilon_{(1)} \tag{44}$$

In every consecutive step k, the modulus E is iterated by modulus:

$$E_{(k)} = \sigma(k-1) / \varepsilon_{(k-1)} \tag{45}$$

The stresses $\sigma_{(n)}$ (the n-th iteration step) are the final solution in the elasto-plastic range. They must satisfy the condition:

$$\left|\sigma_{(n)} - \sigma(n)\right| \le \Delta\sigma \tag{46}$$

where $\Delta\sigma$ is the complex accuracy of solution. Then the plastic strain (permanent) is equal to:

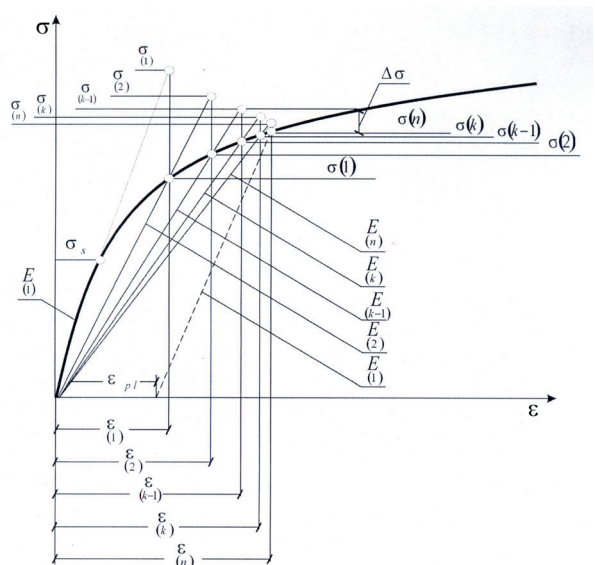$$\varepsilon_{pl} = \sigma(n) / E_{(n)} - \sigma(n) / E_{(1)} \tag{47}$$

Fig. 6. Iteration of elasto-plastic states

6. The examples of computations

6.1. The computations of the temperature field and volumetric phase participations.

Computations of changeable in time temperature field, phase transformations and stress states have been conducted for arc weld surfaced quadratic plate with side length 0.1 m and thickness 0.03 m made from steel S235. Surfacing has been simulated by applying a weld length of 0.1 m in the middle of the plate. Thermal properties of the welded material and the electrode have been determined by $a = 8·10^{-6}$ m²/s, $C_p = 670$ J/(kg K), $\rho = \rho_e = 7800$ kg/m3 and $L = 268$ kJ/kg. Numerical simulations have been conducted for the welding heat source of power 3500 W, which corresponds to the power obtained with welding parameters ($U = 24,3$ V, $I = 232$ A, $\eta = 0.6$) used in the welding experiment presented in [28]. The heat source model for an electric arc with Gaussian distribution of power density is characterized by $z_0 = 0.0062$ m and $t_0 = 0.001$ s. As in the experiment, in calculations there were assumed: welding velocity $v = 0.007$ m/s, electrode wire diameter $d = 1.2$ mm, wire feed speed $v_e = 0.013$ m/s and bead dimensions $h_w = 2.77$ mm and $w_w = 11.93$ mm ($d_p = 0$). The initial value of temperature of electrode T_e=100 °C has been assumed (a temperature of contact tip with the welding head) [19].

Computations have been made for cross-section in the half length of surfaced area. In Figure 7 the distribution of maximum temperature has been presented. Kinetics of phase transformations during heating is limited by the initial and final temperature of austenitic transformation, which are equal to $A_1 = 720$ [°C] and $A_3 = 835$ [°C] respectively. Limits determined by temperatures A_1 and A_3 allow to determine heat affected zone (Fig. 8).
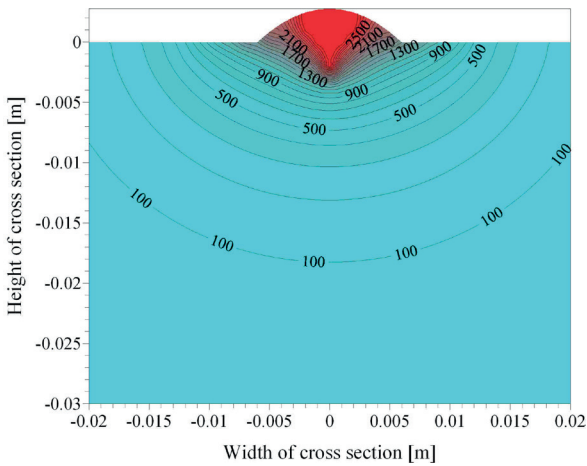
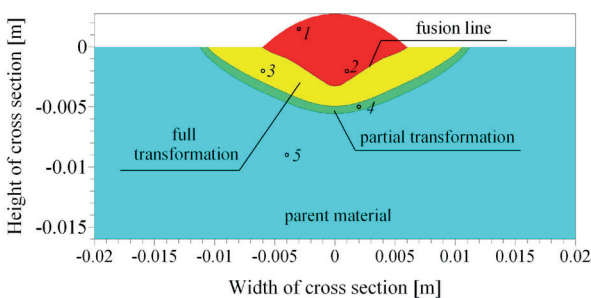Temperature of solidus 1493 °C determines fusion line confirmed experimentally by Klimpel et al. [28]. In the figure selected points of section have been marked, for which analysis of welding thermal cycles, of phase transformations and of stress states has been made further in this work. The progress of phase transformations during cooling has been determined basing on TTT-welding diagram for steel S235 presented in Fig. 9 [29].
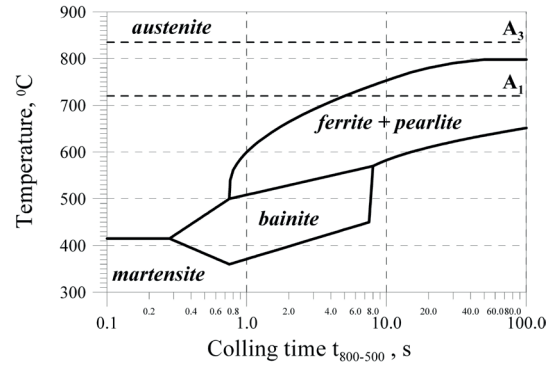

Fig. 9. TTT-welding diagram for S235 steel

In figures 10 – 14 there has been presented the history of temperature changes and volumetric shares of phases for selected cross section points (comp. Fig. 8). Fig. 10 illustrates above mentioned changes for point 1 of section with coordinates (-0.003, 0.00154) from the area of applied weld, therefore thermal cycle and volume phase fractions diagram begins after application of liquid metal. After solidification during cooling, austenite transforms into ferrite, pearlite and bainite. Remaining figures illustrate the history of temperature changes and volume fractions of particular phase for points from fusion zone (Fig. 11), heat affected zone (Fig. 12 and 13) and parent material (Fig. 14). At section points 2 (0.001, -0.002) [m] and 3 (-0.007, -0.002) - Fig. 11 and 12, during heating austenite transforms completely and then as a result of transformation of over-cooled austenite, bainite-ferrite-pearlite structure is created. At section point 4 (0.009, -0.003) [m] (Fig. 13) initial structure partially transforms into austenite. Maximum temperature at this point exceeds initial temperature A_1 of austenitization, but does not reach temperature A_3. At section point 5 (-0.004, -0.009) [m] (Fig. 14) maximum temperature did not exceed initial temperature A_1 of austenitization and material retained original phase composition.

Fig. 7. The distribution of maximum temperature
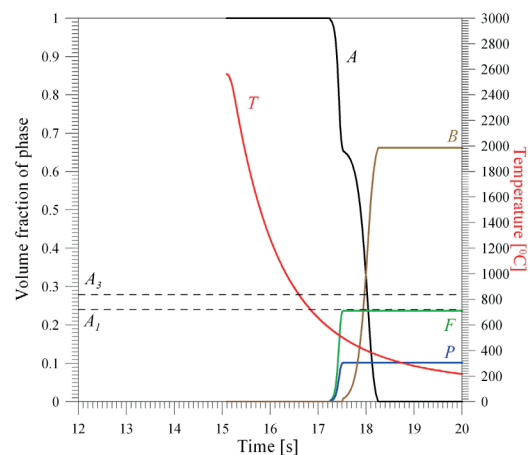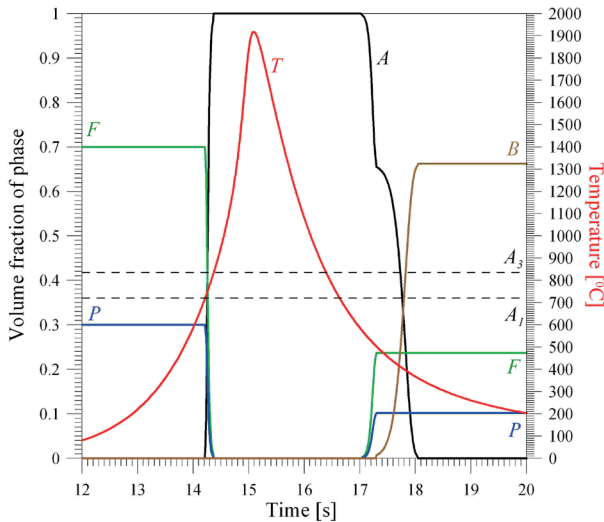

Fig. 8. Heat affected zones

Fig. 10. Thermal cycle and phase volume fraction changes at point 1 of cross section

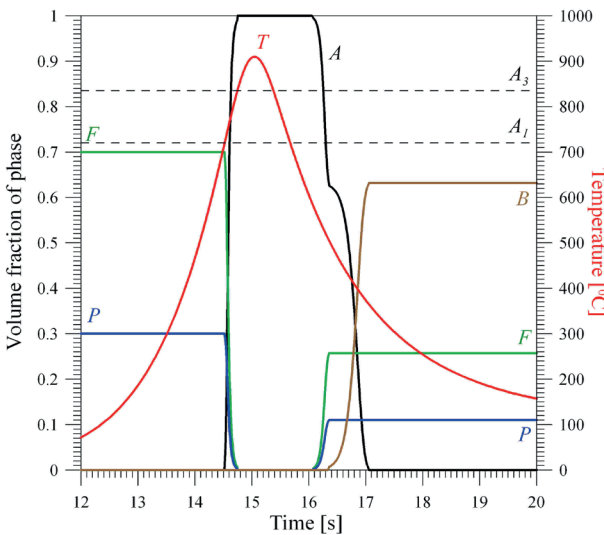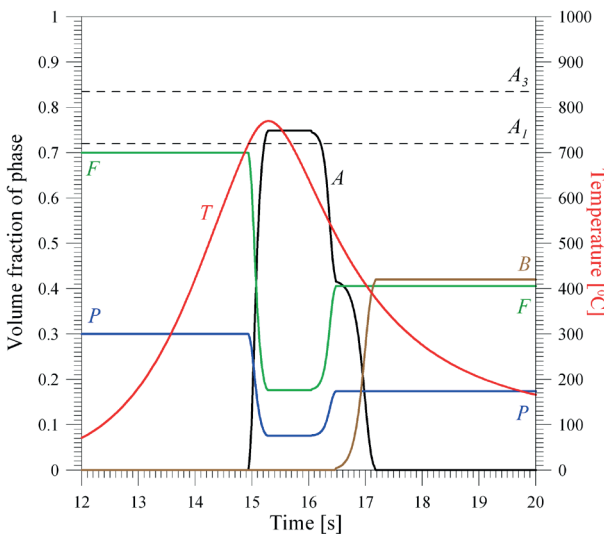Fig. 11. Thermal cycle and phase volume fraction changes at point *2* of cross section
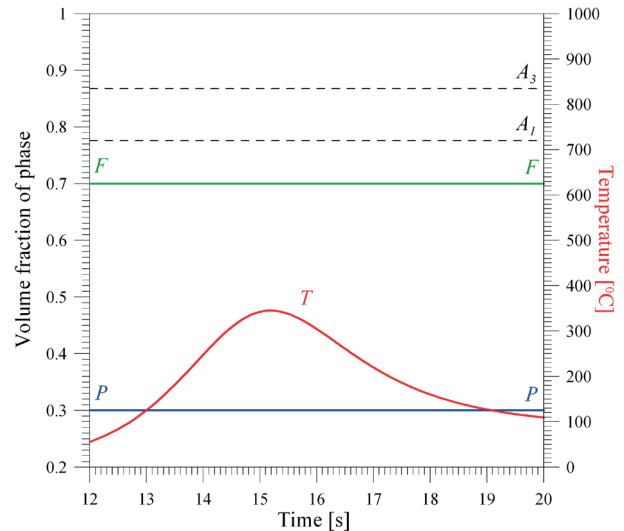

Fig. 14. Thermal cycle and phase volume fraction changes at point *5* of cross section

In strain calculations there was assumed linear expansion coefficients of particular structural elements and structural stresses (Tab. 1) determined on the basis of the author's own dilatometric research [30].

Fig. 12. Thermal cycle and phase volume fraction changes at point *3* of cross section

TABLE 1

Structural (γ) and thermal (α) expansion coefficients of phases

	α [1/°C]		γ
Austenite	$2.178 \cdot 10^{-5}$	$\gamma F,P,S \to A$	$1.986 \cdot 10^{-3}$
Ferrite	$1.534 \cdot 10^{-5}$	$\gamma B \to A$	$1.440 \cdot 10^{-3}$
Pearlite	$1.534 \cdot 10^{-5}$	$\gamma A \to F,P$	$3.055 \cdot 10^{-3}$
Bainite	$1.171 \cdot 10^{-5}$	$\gamma A \to B$	$4.0 \cdot 10^{-3}$
Martensite	$1.36 \cdot 10^{-5}$		

6.2. The analysis of temporary and residual stresses

Tensile curves of ferrite and pearlite are assumed on the basis of works [31, 32]. In case of austenite, bainite and martensite on the basis of data from works [33, 34] tensile curves are determined according to Swift law [35, 36].

Residual stresses distribution in the whole cross-section of the element has been presented in Fig. 15, while the stresses in the middle part of the cross section have been presented in Fig. 16.

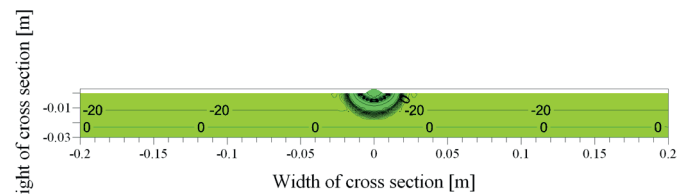Fig. 13. Thermal cycle and phase volume fraction changes at point *4* of cross section

Fig. 15. Residual stress distribution in the whole cross-section of element

Residual stresses distribution is distinguished by high values of tensile stresses in weld and heat affected zones. In the

parent material area (outside heat affected zone) compressive stress state occurs. It should be observed that compressive stresses in the crosswise direction to weld axis at a distance of ca. 5 mm from the axis retain relatively constant value. In vertical direction (regarding the height of section) the value of compressive stresses is higher on the upper surface of element and decreases in the direction of lower surface. Characteristic of these stresses has been experimentally confirmed by Chang et al. [37] and numerically with the use of FEM by Jiang et al. [38].
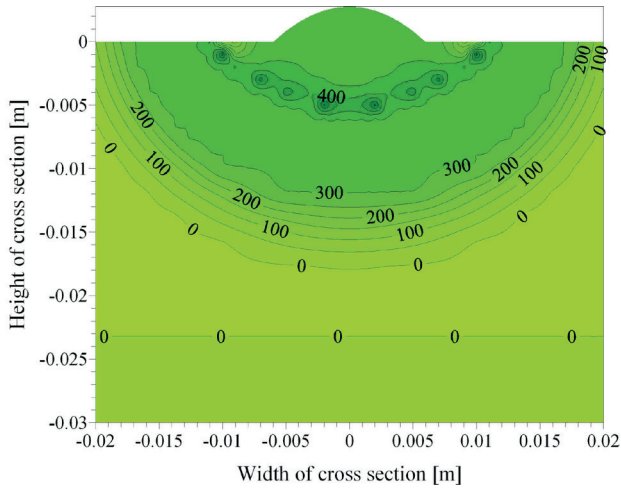

Fig. 16. Residual stresses in the middle part-area of cross section

In fusion and full transformation areas tensile stress values are determined by plastic strains and fractions of phase components. When volume fraction of bainite exceeds 60% and yield stress is much higher than yield stress of ferrite and pearlite, tensile stresses in these areas amount to 560 MPa. In narrow area of partial transformation values of these strains plunge to ca. 350 MPa. In remaining areas of parent material, stress state is determined by maintenance of stress equilibrium in the cross-section.

In figures 17 – 21 the history of stress states changes at selected points of cross section has been presented (comp. Fig. 8). At point *1* from the weld area (Fig. 17), stresses amount to zero as long as the point is in a state of liquid metal. After solidification during cooling tensile stresses increase. Sudden transformation of stresses into compressive between 15 – 20 s is caused by phase transformation. At point *2* from fusion zone (Fig. 18) due to heating compressive stresses increase. During transformation of initial structure into austenite stresses become tensile, but then during melting they vanish. After solidification the history of stress changes is similar to that at point *1*. At point *3* (Fig. 19) from the area of full transformation due to the heating compressive stresses occur. Then, likewise at point *2*, due to transformation of initial structure into austenite, stress state changes into tensile. Next, tensile stresses, being under the influence of further temperature growth, decrease but during

cooling stresses increase again. During phase transformations of overcooled austenite into ferrite, pearlite and bainite stresses plunge becoming compressive. Then during further cooling compressive stresses decrease but values of tensile stresses increase. At point *4* (Fig. 20) from the area of partial transformation during heating compressive stresses increase, but then due to austenitization transform into tensile. During transformation cooling, what causes further, much slower growth of tensile stresses. Transformations during cooling cause the decrease in values of tensile stresses and change of their sign. After phase transformations, due to further cooling, compressive stresses decrease, while tensile start to increase. At point *5* (Fig. 21) from the parent material area change of stress states results from temperature changes, changes of yield stress and from stress equilibrium in the cross-section. Compressive stresses increase during heating but decrease during cooling, becoming tensile.
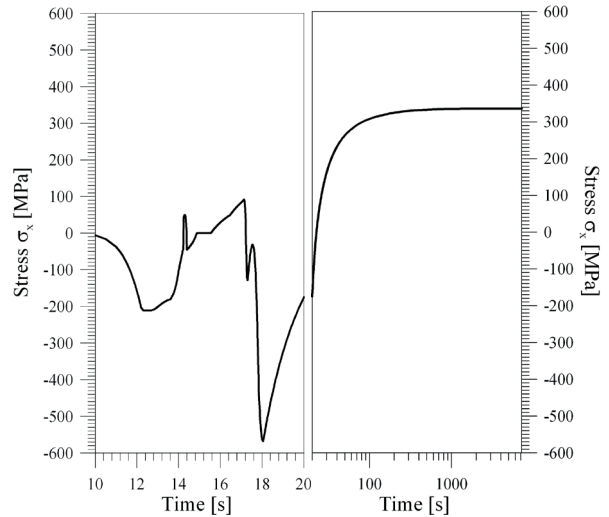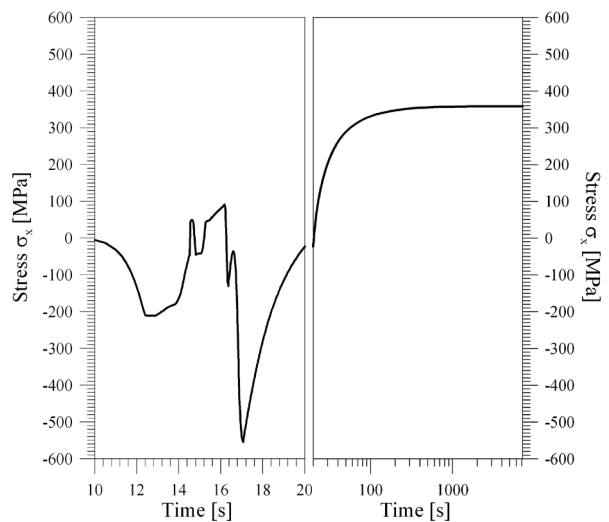

Fig. 18. Stresses during surfacing at point 2

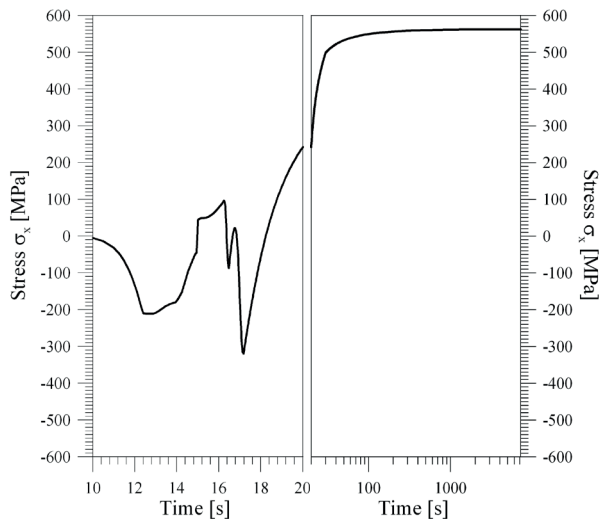Fig. 19. Stresses during surfacing at point 3

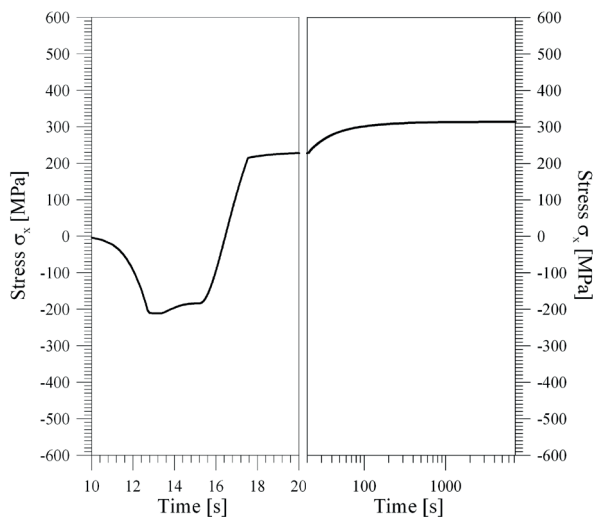Fig. 20. Stresses during surfacing at point 4

Fig. 21. Stresses during surfacing at point 5

7. Conclusions

The performed temperature calculations of single-pass surfacing are confirmed by presented in literature HAZ shapes and fusion lines. Taking into account in the modeling of the temperature field both the thermal radiation from the mobile electrode and the heat of the molten electrode material allows more precise reproduction of the shape of the fusion line. As the result of the determination of variable temperature fields, heating phase transformation defined by the initial and final temperatures of austenite transformation were considered, subjecting them to the chemical composition of the steel, whereas the cooling phase transformations – on the basis of CCT-S diagrams.

Calculated state of residual normal stresses after arc weld surfacing is characterised by high values of tensile stresses in weld, fusion and full transformation zones as well as by a sudden decrease of their values in partial transformation zone. Whereas in parent material areas outside heat affected zone in perpendicular direction to the weld axis compressive stresses with almost constant values occur. Correctness of such residual stress distribution was proved by experimental results presented in literature.

The obtained results of numerical simulations confirm the correctness of models and author's programs. They provide the basis for modeling of multiple-surfacing used in industrial practice.

REFERENCES

[1] E. Tasak, Metallurgy of welding, JAK, Cracov 2008.

[2] D. Radaj, Heat effects of welding. Temperature field, residual stress, distortion, Springer-Verlag, Berlin 1992.

[3] J. Pilarczyk, J. Pilarczyk, Arc welding and surfacing of metals, Slask sp. z o.o., Katowice 1996.

[4] A. Bokota, S. Iskierka, Numerical analysis of phase transformations and residual stresses in steel cone-shaped elements hardened by induction and flame methods, Int. J. Mech. Sci. **40**, 6, 617 – 629 (1998).

[5] L.E. Lindgren, Computational welding mechanics, Woodhead Publishing and Maney Publishing, Cambridge 2007

[6] B. Chen, X.H. Peng, J.H. Fan, S.T. Sun, A viscous-elastoplastic constitutive equation incorporating phase transformation with the application to the residual stress analysis for welding process, J. Mater. Proces. Technol. **205**, 316-321 (2008).

[7] D. Deng, FEM prediction of welding residual stress and distortion in carbon steel considering phase transformation effects, Materials Design **30**, 359-366. (2009).

[8] J.A. Goldak, M. Akhlaghi, Computational welding mechanics, Springer, New York 2010.

[9] W. Piekarska, M. Kubiak, Z. Saternus, Numerical simulation of deformations in T-joint welded by the laser beam, Arch. Metall. Mater. **58,** 1391 – 1396 (2013).

[10] N.T. Nguyen, Thermal analysis of welds, WITPress, Southampton, Boston 2004.

[11] P. Lacki, K. Adamus, Numerical simulation of the elektron beam welding process, Computers and Structures **89**, 977 – 985 (2011).

[12] W. Piekarska, M. Kubiak, Theoretical investigations into heat transfer in laser-welded steel sheets, J. Them. Anal. Calorim **110**, 159 – 166 (2012).

[13] S. Joshi, J. Hildebrand, A.S. Aloraier, T. Rabczuk, Characterization of material properties and heat source parameters in welding simulation of two overlapping beads on a substrate plate, Comput. Mater. Sci. **69**, 559-565 (2013).

[14] A. Ghosh, N. Barman, H. Chattopadhyay, S. Hloch, A study of thermal behaviour during submerged arc welding, Strojniški vestnik – J. Mech. Eng., **59** (5), 333 – 338 (2013).

[15] P. Hrabe, R. Choteborsky, M. Navratilova, Influence of welding parameters on geometry of weld deposit bead. In: Int. Proc. Conf. Economic Eng. Manufacturing Systems, Brasov, Regent, 10 3(27) 291-294 (2009).

[16] J. Winczek, Analytical solution to transient temperature field in a half-infinite body caused by moving volumetric heat source, Int. J. Heat Mass Transfer **53**, 5774-5781 (2010).

[17] J. Winczek, New approach to modeling of temperature field in surfaced steel elements, Int. J. Heat Mass Transfer, **54**, 4702–4709 (2011).

[18] P.R. Vishnu, W.B. Li, K.E. Easterling, Heat-flow model for pulsed welding, Mater. Sci. Techn. **7**, 649-659 (1991).

[19] P.J. Modenesi, R.I. Reis, A model for melting rate phenomena in GMA welding, J. Mater. Proc. Technol. **189**, 199-205 (2007).

[20] W. Piekarska, M. Kubiak, A. Bokota, Numerical simulation of thermal phenomena and phase transformations in laser-arc hybrid welded joint, Archives of Metallurgy and Materials **56**, 409-421 (2011).

[21] M. Avrami, Kinetics of phase change. I. General theory, J. Chem. Physics, **7**, 1103-1112 (1939).

[22] R. Parkitny, J. Winczek, Modelling of phase transformations during multipass surfacing, In:. Conf. Proc. XXXVIII Sympozjon Modelling in Mechanics, Silesian University of Technology, Gliwice, 219-224 (1999).

[23] D.P. Koistinen, R.E. Marburger, A general equation prescribing the extent of the austenite-martensite transformation in pure iron-carbon alloys and plain carbon steels, Acta Metall. **7** 59-60 (1959).

[24] A. Bokota, T. Domański, Numerical analysis of thermo-mechanical phenomena of hardening process of elements made of carbon steel C80U, Arch. Metall. Mater. **52**, 277 – 288 (2007).

[25] T. Domański, A. Bokota, Numerical models of hardening phenomena of tools steel base on the TTT and CCT diagrams, Arch. Metall. Mater. 56, 325 – 344 (2011).

[26] J. Winczek, A simplified method of predicting stresses in surfaced steel rods, J. Mater. Proc. Techn. **212,** 1080 – 1088 (2012).

[27] A. Bokota, R. Parkitny, Modelling of thermal, structural and mechanical phenomena in hardening processes of steel elements. In: Informatics in Metal Technology, Silesian University of Technology, Gliwice, 257 – 298 (2003).

[28] A. Klimpel, M. Balcer, A.S. Klimpel, A. Rzeźnikiewicz, The effect of the method and parameters in the GMA surfacing with solid wires on the quality of pudding welds and the content of the base material in the overlay, Welding Int. **20**, 845-850 (2006).

[29] J. Brózda, J. Pilarczyk, M. Zeman, TTT-welding diagrams transformation of austenite, Śląsk, Katowice 1983.

[30] J. Winczek, A. Kulawik, Dilatometric and hardness analysis of C45 steel tempering with different heating-up rates, Metalurgija, **51** (1), 9 – 12 (2012).

[31] J. Gawąd, D. Szeliga, A. Bator, V. Pidvysockyy, M. Pietrzyk, Interpretation of the tensile test results interpretation based on two criterion optimization, In: Proc. 14. Conf. KomPlasTech, Informatics in Metal Technology, ed. M. Pietrzyk et al., Akapit, Cracow, 27-34 (2004).

[32] P.M.M. Vila Real, R. Cazeli, L. Simoes da Silva, A. Santiago, P. Piloto, The effect of residual stresses in the lateral-torsional buckling of steel I-beams at elevated temperature, J. Construct. Steel Research **60**, 783-793 (2004).

[33] M. Melander, A compitional and experimental investigation of induction and laser hardening, Linkoping Studies in Science and Technology, Dissertation No 124, Linkoping Univeristy (1985).

[34] J. Lian, Z. Jiang, J. Liu, Theoretical model for the tensile work hardening behaviour of dual-phase steel, Mater. Sci. Eng. **A147**, 55 – 65 (1991).

[35] S.K. Kim, Y.M. Kim, Y.J. Lim, N.J. Kim, Relationship between yield ratio and the material constants of the swift equation, Metals Materials Int. **12**, No 2 131-135 (2006).

[36] J. Winczek, The analysis of stress states in steel rods surfaced by welding, Archiv. Metall. Mater. **58**, 1243 – 1252 (2013).

[37] P.H. Chang, T.L Teng, Numerical and experimental investigations on the residual stresses of the butt-welded joints, Comput. Mater.Sci. **29**, 511 –522 (2004).

[38] W. Jiang, Z. Liu, J.M. Gong, S.T. Tu, Numerical simulation to study the effect of repair width on residual stresses of stainless steel clad plate, Int. J. Pres. Ves. Pip. **87**, 457 – 463 (2010).